An exploratory examination of the electron density and electrostatic potential of phenakite

James W. Downs,* G. V. Gibbs

Department of Geological Sciences, Virginia Polytechnic Institute and State University, Blacksburg, Virginia 24061, U.S.A.

Abstract

The deformation electron density and total electrostatic potential of phenakite, Be_2SiO_4, are retrieved from single-crystal X-ray diffraction intensities. Refinements are completed using several models, including a flexible pseudoatom model wherein the electron density about each nucleus is represented by a short multipole expansion. Associated with each nearest-neighbor Be–O and Si–O interatomic vector is an accumulation of deformation density. Short bonds have greater deformation-density accumulation than do long bonds between similar atoms. The topography of the deformation density about each oxygen indicates, in a qualitative sense, both ionic and covalent contributions to the bonding.

Introduction

The crystal structure of phenakite was solved by Bragg and Zachariasen (1930), refined under room conditions by Zachariasen (1972), at elevated temperatures by Hazen and Finger (1987), and at high pressures by Hazen and Au (1986) and Kogure and Takéuchi (1986). Phenakite crystallizes in space group $R\bar{3}$ with all atoms on general positions. The two nonequivalent Be and one Si in the unit cell are each 4-coordinated by oxygen atoms. The four unique oxygen atoms in the unit cell are each bonded to two Be and one Si atom disposed at the corners of a triangle. The coordination triangles about O(1), O(3), and O(4) parallel the Z axis (Fig. 1), whereas the coordination triangle about O(2) lies in a plane perpendicular to the Z axis.

As a logical extension of the work of Zachariasen (1972), we have attempted to obtain accurate X-ray structure-factor moduli for phenakite from which the details of the electron-density distribution may be retrieved. Although our results are rather crude compared to those that could be obtained from the true, but unknown, electronic wave-function for phenakite, they represent a first attempt to relate the structural details of this material to the experimentally observed one-electron density function. Since the cohesive energy is a functional of the one-electron density (Hohenberg and Kohn, 1964), and all interatomic forces may be obtained via classical electrostatics from the charge density (Feynman, 1939), it behooves us to earnestly begin to examine the detailed charge-density distributions of minerals.

This paper is divided into four sections. The first deals with the details of data collection, reduction, and our observations as to the accuracy of the data. Next, the results of various levels of least-squares refinement of the

electron-density model are discussed. These include refinements using neutral, spherical-atom scattering factors, a kappa refinement, and finally a refinement wherein the electron density of each atom is expanded in a short multipole expansion. Maps of deformation electron density and total electrostatic potential are then examined (Downs, 1983).

Experimental details

A colorless crystal of phenakite from San Miguel di Piraciaba, Brazil, was obtained from the U.S. National Museum, Smithsonian Institution (USNM no. B21152). A fragment with approximate dimensions $0.08 \times 0.07 \times 0.07$ mm was mounted in a general orientation on a glass fiber. The crystal is bounded by six planes, and the distance of each face from the centroid of the crystal was measured using an image-splitting eyepiece while the goniometer head and crystal were mounted on a spindle stage. The crystal was optically centered on a Picker four-circle diffractometer, automated with a Krisel control system, and the diffractometer angles to bring each of the faces into diffracting position were carefully measured. These data were used in the calculation of the transmission factors and the absorption-weighted mean-path lengths for each reflection. Crystal centering, tube height, and angle zeros were checked on a high-angle reflection using Hamilton's method (Hamilton, 1974).

Information pertinent to data collection and reduction are given in Table 1. Unit-cell dimensions and an orientation matrix were refined by least-squares methods from the corrected angles of the $MoK\alpha_1$ peak for 17 reflections with 2θ in the range 60–72°. All Bragg reflections with $\sin\theta/\lambda < 1.0$ within the sphere of reflection consistent with space group $R\bar{3}$ were step-scanned. Reflection profiles were reduced to integrated intensities using the method of Lehmann and Larsen (1974) as incorporated in the profile-analysis program of Blessing et al. (1974). During this procedure, special care was taken to account properly for the effect of the Zr-filter attentuation for low-angle reflections. Line-printer profiles for all reflections with $I > 2\sigma(I)$ were plotted and checked for possible profile-analysis errors. For several weak reflections, the $K\alpha_2$ peak had been included in the high-order background during the Lehmann-Larsen procedure. Intensities for

---

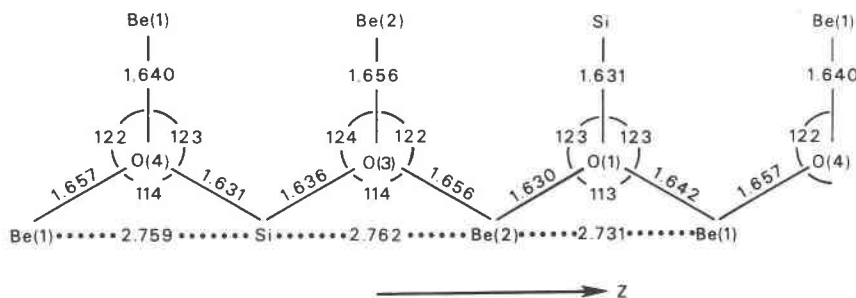* Present address: Department of Geology and Mineralogy, Ohio State University, Columbus, Ohio 43210, U.S.A.

Fig. 1. Phenakite structure in plane containing triangular-coordinated oxygen atoms. The Z axis is horizontal; distances are in ångströms; angles are in degrees.

these reflections were recomputed by setting the limits of the Bragg peak to one-sixth from each end of the scan. A similar procedure was used for all reflections within $I < 2\sigma(I)$. Three standard reflections were step-scanned every 8 h, resulting in 272 sets of standards with an internal-agreement factor of 0.5%. All intensities were corrected for Lorentz, polarization, and absorption effects.

Owing to the small crystal size and intensity limitations of the sealed-tube radiation source, 54% of the measured intensities had $I < 3\sigma(I)$ and were assumed to be unobserved. A small crystal was chosen deliberately in an attempt to minimize secondary extinction. Integrated intensities with $I > 3\sigma(I)$ were averaged in Laue groups $\bar{3}$ and $\bar{1}$ (Table 1). The relatively poor internal agreement among symmetry-equivalent intensities for Laue group $\bar{3}$ could not be rationalized by invoking either path-dependent isotropic extinction or anisotropic extinction. Therefore, data averaged in group $\bar{3}$ were used in subsequent refinements, and the extinction model was limited to the isotropic case.

These data would be considered almost ideal for electron-density analysis if the agreement among symmetry equivalents was around 1% and extinction on any structural amplitude did not exceed 5%. Under such conditions, it could be possible to retrieve a very reliable electron-density distribution from the data. Because of the fairly large internal-agreement factors, however, the integrated intensities used in the current study cannot be considered to be extremely accurate and must be used with caution. We will see that these intensities, although not ideal for electron-density analysis, nevertheless yield electron-density features that appear to be consistent with the structural details of phenakite. We thus consider the present result as a first attempt to map the electrostatic properties of this material.

ELECTRON-DENSITY MODEL REFINEMENTS

All refinements were completed using the VALRAY system (Stewart and Spackman, 1983). Anomalous scattering terms for Si and oxygen were taken from Cromer and Liberman (1970), and extinction was modeled as mosaic-spread-dominated (Type I) with a Lorentzian mosaic-distribution function within the formalism of Becker and Coppens (1974a, 1974b). All refinements were based on $|F|^2$ with weights computed from Poisson counting statistics and averaging statistics with no ignorance factor. During the final cycle of each refinement, second derivatives were included in the Hessian matrix to insure that a true minimum had been located and to improve error estimates. The figures of merit from the final refinement cycle for each model are given in Table 2.

IAM model

In conventional crystal-structure analysis, a scale factor, positional parameters, vibrational parameters, and extinction parameters may be refined, whereas the atomic scattering factors are assumed to be known a priori. A scattering model of noninteracting, neutrally charged, spherically averaged atoms is often chosen. This is the independent atom model (or IAM). For conventional work, the IAM is an excellent choice, since a large part of the binding between atoms can be traced to the electrostatic attraction between independent atoms (Hirshfeld and Rzotkiewicz, 1974). In this study, scattering factors for each reflection were computed directly from the spherically averaged Hartree-Fock atomic wavefunctions of Clementi and Roetti (1974). The figures of merit for the IAM refinement are quite reasonable for a conventional model.

GSF model

As a first step toward improving the electron-density model, one may choose scattering factors that begin to model interacting atoms. Form factors for half-ionized or fully ionized atoms are often used for this purpose. In an a priori attempt to find scattering factors that mimic bonded atoms, we have chosen the monopole terms of

TABLE 1. Crystallographic data

Space group	$R\bar{3}$	
Unit-cell dimensions:		
a (Å)	12.472(2)	
c (Å)	8.251(1)	
Radiation	Zr-filtered Mo$K\alpha$	
Scan type	θ–2θ step scans	
Step size (°)	0.04	
Time per step (s)	10	
Scan width (°)	$\Delta2\theta = 2.0 + 0.7 \tan\theta$	
$\sin\theta/\lambda$ range (Å^{-1})	0.08–1.0	
No. reflections measured	11 700	
No. refs. with $I > 3\sigma(I)$	6299	
Absorption coefficient (cm^{-1})	7.088	
Range of transmission factors	0.946–0.957	
Averaging statistics for $I > 3\sigma(I)$:		
Laue group	$\bar{3}$	$\bar{1}$
$R = \Sigma|F_o^2 - F_{avg}^2|^2/\Sigma F_o^2$	0.041	0.021
No. observations	1053	3330

TABLE 2. Figures of merit from least-squares refinements

	IAM	GSF	Kappa	Multipole
k	1.009(2)	1.012(2)	1.062(5)*	1.005(1)*
g	2.65(5)	2.64(4)	3.44(4)	2.83(2)
y_{min}	0.51	0.51	0.47	0.49
N_o	1 053	1 053	1 053	1 053
N_v	65	65	79	176
ϵ	21 606	15790	9583	2952
$R(F^2)$	0.0308	0.0292	0.0269	0.0184
$R_w(F^2)$	0.0462	0.0395	0.0308	0.0171
S	4.676	3.998	3.137	1.834

$$|F_o|^2 = k^2 y |F_{kin}|^2$$
$$\epsilon = \Sigma \, w(|F_o|^2 - k^2|F_c|^2)^2$$
$$R(|F|^2) = (\Sigma \, ||F_o|^2 - k^2|F_c|^2|/\Sigma \, |F_o|^2)^{1/2}$$
$$R_w(|F|^2) = (\epsilon/\Sigma \, |F_o|^4)^{1/2}$$
$$S = [\epsilon/(N_o - N_v)]^{1/2}$$

Note: N_o = number of observations, N_v = number of variables.
* Effective scale factor $k = (\Sigma \, P_o)/F(000)$, where P_o = monopole population.

TABLE 3. Kappa charges and kappa parameters

Atom	q	κ
Si	+1.49(5)	1.13(2)
Be(1)	+1.16(1)	1.32(6)
Be(2)	+1.38(1)	1.33(8)
O(1)	−0.915(3)	0.934(5)
O(2)	−1.103(3)	0.916(4)
O(3)	−0.913(4)	0.932(5)
O(4)	−1.095(4)	0.923(5)

small multipole expansions of the molecular form factors of appropriate diatomic molecules. These *generalized scattering factors* (or GSFs) are discussed in detail by Stewart et al. (1975). For phenakite, the monopole GSFs for Be and Si were computed from the one-electron density functions of the BeO and SiO diatomics, respectively. The oxygen monopoles from the SiO, BeO, NaO, LiO, BO, CO, NO, ClO, O_2, OH^-, OF^- diatomics, and the O^- ion were used to construct an oxygen monopole to yield a charge-balanced system. The resulting GSFs have *monopole charges* of +1.213, +1.322 and −0.937 for Be, Si, and oxygen respectively. The figures of merit indicate a significantly improved least-squares fit using GSFs relative to IAM scattering factors.

Kappa model

Under favorable conditions, the monopole terms may be included as refinable parameters. The most widely used *monopoles only* refinement is the *kappa refinement* (Coppens, 1977). In this model the scattering factor for each atom is split into separate *core* and *valence* parts. The core- and valence-electron populations are allowed to vary. Furthermore, the valence scattering factor is scaled by an additional parameter, kappa, which allows the valence shell of the atom to expand or contract. In a kappa refinement, the scattering factor for each atom is given by

$$f(s) = P_{core}f_{core}(s) + P_{valence}f_{valence}(s/\kappa),$$

where $s = 2 \sin \theta/\lambda$, the magnitude of the Bragg vector. These scattering factors retain spherical symmetry in reciprocal space. P_{core} and $P_{valence}$ are, respectively, the core- and valence-electron populations and f_{core} and $f_{valence}$ are the appropriate scattering factors normalized to unity. If $\kappa > 1$, the valence shell is contracted relative to the valence shell of the isolated atom. If $\kappa < 1$, the valence shell is expanded. The choice of f_{core} and $f_{valence}$ is not unique, and different functions will yield different electron populations. We have chosen the density-localized shell scattering factors of Stewart (1980) as tabulated in Stewart

and Spackman (1983). These functions ensure that virtually all of the electron density on the nucleus arises from the core function. If canonical rather than localized orbitals are used for Be, then a substantial amount of the core density comes from the 2s valence orbital.

During the kappa refinement, the core populations were varied, but constrained so that the Be and oxygen core populations were each $\frac{1}{5}$ that of Si. No scale factor is refined during the kappa refinement, but an effective scale factor is obtained from the sum of the monopole populations (i.e., P_{core} and $P_{valence}$) divided by the number of electrons in the unit cell. The sum of the core and valence populations on each atom, scaled by the effective scale factor, can be subtracted from the number of electrons in the neutral atom to yield what is known as a *kappa charge,* the atomic charge obtained from a kappa refinement. Kappa charges and kappa parameters for each atom are given in Table 3. As expected, relative to isolated atoms, Si and Be become positively charged and contracted, and each oxygen becomes negatively charged and expanded. The valence-electron populations of Si and Be are much less well determined than for oxygen. This stems from the fact that the valence functions of Si and Be are very diffuse in direct space, yielding valence scattering factors that are highly contracted in reciprocal space. Since only a small number of reflections sample that part of reciprocal space in which the Si and Be valence scattering factors have large amplitude, these populations are often difficult to determine. The figures of merit (Table 2) for the kappa refinement show a fit substantially better than the IAM or GSF refinement.

We wish to emphasize that the kappa charges from Table 3 should *not* be interpreted as the experimentally *observed* atomic charges for phenakite for use in either theoretical models or as a measure of ionicity. The valence functions, which are populated to obtain the kappa charge, have substantial amplitude on neighboring nuclei and beyond. The purpose of the kappa refinement is to provide a more flexible and realistic model for the *total* electron distribution. Most attempts to partition this distribution into atomic properties (.e.g., charges) can be considered as arbitrary. A rigorous, quantum mechanically sound method for obtaining *atoms* from molecules are the virial fragments of Bader (1981), which are based upon the topography of the gradient of the total electron density. However, these atomic fragments are generally

TABLE 4. Positional and apparent vibrational parameters from multipole model

Para-meter	Si	Be(1)	Be(2)	O(1)	O(2)	O(3)	O(4)
x	0.19562(2)	0.1943(1)	0.1941(1)	0.20975(8)	0.33382(9)	0.12223(7)	0.12228(7)
y	0.98402(2)	0.9841(1)	0.9822(1)	0.12125(8)	0.00040(9)	0.91217(7)	0.91342(7)
z	0.74990(3)	0.4156(1)	0.0846(1)	0.7503(1)	0.74991(6)	0.91497(8)	0.58495(8)
U_{11} (Å^2)	0.0035(1)	0.0052(6)	0.0045(5)	0.0075(3)	0.0027(3)	0.0043(3)	0.0040(3)
U_{22} (Å^2)	0.0030(1)	0.0055(6)	0.0056(5)	0.0042(3)	0.0044(3)	0.0047(3)	0.0047(3)
U_{33} (Å^2)	0.00300(6)	0.0048(5)	0.0053(5)	0.0036(3)	0.0059(2)	0.0035(2)	0.0035(2)
U_{12} (Å^2)	0.00141(9)	0.0026(5)	0.0023(5)	0.0037(3)	0.0017(3)	0.0014(2)	0.0010(2)
U_{13} (Å^2)	0.00005(9)	−0.0005(5)	−0.0001(4)	0.0000(2)	−0.0002(3)	0.0003(2)	−0.0002(2)
U_{23} (Å^2)	0.00014(9)	0.0003(5)	−0.0000(4)	−0.0003(2)	−0.0003(3)	0.0001(2)	−0.0003(2)
B_{eq} (Å^2)*	0.26(1)	0.41(4)	0.41(3)	0.38(2)	0.34(2)	0.36(2)	0.36(2)

* $B_{eq} = (8\pi^2/3)[(4/3)(U_{11} + U_{22} - U_{12}) + U_{33}]$.

not spherical, or even approximately so, and therefore do not satisfy our conventional picture of atoms.

Multipole model

In our final structure-factor model, the scattering factor of each pseudoatom is expanded in a small multipole expansion after the manner of Stewart (1976). The multipole model for phenakite consists of the GSFs as fixed monopoles, with three dipoles, five quadrupoles, and seven octopoles to complete each pseudoatom. Attempts to refine monopole populations and kappas together with higher multipoles failed to converge. The higher multipoles each consist of a radial function of the form $r^n e^{-\alpha r}$ and an angular function given by the appropriate tesseral harmonic. Angular functions for all pseudoatoms are defined relative to the same coordinate system. Furthermore, all higher multipoles on each pseudoatom are constrained to share the same radial exponent. Since the multipole expansion now contains angularly dependent functions, the scattering factor for each pseudoatom now varies not only with the magnitude but with the direction of the Bragg vector. The agreement factors show the multipole model to give the best fit to the observations. Even with the increased number of parameters, the goodness of fit is seen to most nearly approach the expected value of 1.0.

By far the most extinction-affected observation is the 006 intensity, which is attenuated by about 50%. The extinction *correction* to this observation is given in Table 2 and is seen to vary depending on the structure-factor model. Table 4 lists the positional and apparent vibrational parameters from the multipole refinement, Table 5 gives selected interatomic distances and angles, and Table 6[1] lists the observed and calculated structure-factor moduli.

ELECTROSTATIC PROPERTIES

Deformation density

A map of the vibrationally averaged deformation electron density in the plane of Figure 1 is shown in Figure

[1] To obtain a copy of Table 6, order Document AM-87-346 from the Business Office, Mineralogical Society of America, 1625 I Street, N.W., Suite 414, Washington, D.C. 20006, U.S.A. Please remit $5.00 in advance for the microfiche.

2A. This map is calculated from a three-dimensional Fourier series, where the Fourier coefficients are the difference between the observed structure-factor moduli and those computed from neutral, spherical atoms (i.e., $F_o - F_{IAM}$). The positional and vibrational parameters for the IAM, and the phases for observed reflections are from the multipole refinement. Maps of the deformation density are virtually free of series-termination error since the observed and calculated structure-factor moduli are virtually identical for high-angle reflections that depend mainly upon the distribution of the core electrons. The estimated standard deviation in the deformation density for this plane is given in Figure 2B.

The solid contours in the deformation-density map represent an accumulation of electron density relative to a superposition of isolated atom densities. The dashed contours are negative and show regions where a superposition of isolated atoms gives more electron density than actually observed in the crystal. An examination of the nearest-neighbor interatomic vectors around each oxygen atom shows an accumulation of electron density associated with each of these vectors.

It is of interest to qualitatively compare the magnitude of the electron-density accumulation in the bonds with the observed bond distances. The Si–O(1) and Si–O(4) distances are both 1.631 Å and show electron-density accumulations of similar magnitude. The Si–O(3) distance is 1.636 Å, and the bond shows less deformation density. The Be(1)–O(1) bond, the Be(2)–O(1) bond, and the Be(1)–O(4) bond that is perpendicular to Z are all short in comparison to the Be(2)–O(3) bonds and the Be(1)–O(4) bond that is nearly along Z. As with the Si–O bonds, the short Be–O bonds all show greater accumulation of deformation density than do long Be–O bonds.

The significance of an accumulation of deformation density between bonded atoms should be clarified. Although often used synonymously, the terms *bonding* and *binding* have different meanings to chemists (Berlin, 1951; Bader, 1981). *Bonding* refers to energy changes connected with molecule formation, whereas *binding* refers to interatomic forces. At this point in time, one cannot, in an exact manner, quantitatively study *bonding* from the electron density since the universal functional that relates the one-electron density function to the electronic energy

TABLE 5. Selected interatomic distances and angles

Si tetrahedron		Be(1) tetrahedron		Be(2) tetrahedron	
Si–O(1)[A]	1.631(1)	Be(1)–O(1)[G]	1.642(1)	Be(2)–O(1)[G]	1.630(1)
–O(2)[A]	1.631(1)	–O(2)[F]	1.639(2)	–O(2)[I]	1.638(2)
–O(3)	1.636(1)	–O(4)	1.657(1)	–O(3)[C]	1.656(1)
–O(4)	1.631(1)	–O(4)[K]	1.640(2)	–O(3)[K]	1.656(2)
Mean	1.632	Mean	1.645	Mean	1.645
O(1)[A]–O(2)[A]	2.645(2)	O(1)[G]–O(2)[F]	2.678(1)	O(1)[G]–O(1)[I]	2.679(1)
O(1)[A]–O(3)	2.644(1)	O(1)[G]–O(4)	2.766(1)	O(1)[G]–O(3)[C]	2.762(1)
O(1)[A]–O(4)	2.635(1)	O(1)[G]–O(4)[K]	2.663(1)	O(1)[G]–O(3)[K]	2.658(1)
O(2)[A]–O(4)	2.669(1)	O(2)[F]–O(4)	2.676(1)	O(2)[I]–O(3)[C]	2.678(1)
O(2)[A]–O(4)	2.670(1)	O(2)[F]–O(4)[K]	2.660(1)	O(2)[I]–O(3)[K]	2.656(1)
O(3)–O(4)	2.723(1)	O(4)–O(4)[K]	2.665(1)	O(3)[C]–O(3)[K]	2.676(1)
Mean	2.664	Mean	2.685	Mean	2.685
O(3)–Si–O(4)	112.95(3)	O(4)–Be(1)–O(2)[F]	108.6(1)	O(3)[C]–Be(2)–O(1)[G]	114.37(8)
O(3)–Si–O(1)[A]	108.10(4)	O(4)–Be(1)–O(1)[G]	113.96(8)	O(3)[C]–Be(2)–O(2)[I]	108.8(1)
O(3)–Si–O(2)[A]	109.60(4)	O(4)–Be(1)–O(4)[K]	107.9(1)	O(3)[C]–Be(2)–O(3)[K]	107.8(1)
O(4)–Si–O(1)[A]	107.78(4)	O(2)[F]–Be(1)–O(1)[G]	109.4(1)	O(1)[G]–Be(2)–O(2)[I]	110.1(1)
O(4)–Si–O(2)[A]	109.88(4)	O(2)[F]–Be(1)–O(4)[K]	108.43(7)	O(1)[G]–Be(2)–O(3)[K]	108.0(1)
O(1)[A]–Si–O(2)[A]	108.40(5)	O(1)[G]–Be(1)–O(4)[K]	108.5(1)	O(2)[I]–Be(2)–O(3)[K]	107.48(8)
Mean	109.45	Mean	109.47	Mean	109.42

O(1) triangle		O(2) triangle	
O(1)–Si[D]	1.631(1)	O(2)–Si[D]	1.631(1)
–Be(2)[L]	1.630(1)	–Be(1)[J]	1.639(2)
–Be(1)[L]	1.642(1)	–Be(2)[E]	1.638(2)
Mean	1.634	Mean	1.636

Angles about O(1)		Angles about O(2)	
Si[D]–O(1)–Be(1)[L]	123.30(8)	Si[D]–O(2)–Be(2)[E]	120.33(7)
Si–O(1)–Be(2)[L]	123.34(8)	Si[D]–O(2)–Be(1)[J]	120.17(9)
Be(1)[L]–O(1)–Be(2)[L]	113.1(1)	Be(2)[E]–O(2)–Be(1)[J]	119.5(1)
Mean	119.91	Mean	120.00

O(3) triangle		O(4) triangle	
O(3)–Si	1.636(1)	O(4)–Si	1.631(1)
–Be(2)[H]	1.656(1)	–Be(1)	1.657(1)
–Be(2)[B]	1.656(2)	–Be(1)[H]	1.640(2)
Mean	1.649	Mean	1.643

Angles about O(3)		Angles about O(4)	
Si–O(3)–Be(2)[B]	114.06(5)	Si–O(4)–Be(1)	114.10(5)
Si–O(3)–Be(2)[H]	123.61(6)	Si–O(4)–Be(1)[H]	123.49(5)
Be(2)[B]–O(3)–Be(2)[H]	122.07(7)	Be(1)–O(4)–Be(1)[H]	122.21(7)
Mean	119.91	Mean	119.93

Selected metal-metal distances

Along Z		Others	
Si–Be(1)	2.759(1)	Be(1)–Si[H]	2.880(1)
Si–Be(2)[B]	2.762(1)	Be(1)[H]–Be(1)	2.887(1)
Be(1)–Be(2)[G]	2.731(1)	Be(2)[L]–Si[D]	2.870(1)
Mean	2.751	Be(2)[B]–Be(2)[H]	2.898(1)
		Si–Be(1)[H]	2.881(1)
		Si–Be(2)[H]	2.901(1)
		Mean	2.886

Symmetry code:
[A] $x, 1 + y, z$
[B] $x, y, 1 + z$
[C] $x, y, z - 1$
[D] $x, y - 1, z$
[E] $4/3 - y, x - y + 2/3, 2/3 + z$
[F] $1/3 - y, x - y + 2/3, z - 1/3$
[G] $y, y - x + 1, 1 - z$
[H] $y - 1, y - x, 1 - z$
[I] $y - x + 2/3, 4/3 - x, z - 2/3$
[J] $y - x - 1/3, 1/3 - x, 1/3 + z$
[K] $x - y + 1, x + 1, 1 - z$
[L] $x - y + 1, x, 1 - z$

is not yet fully known. However, through the Hellman-Feynman theorem (Feynman, 1939), questions of chemical *binding* can be approached rigorously given a knowledge of the electron-density distribution.

For diatomic molecules the effect of the electron density on chemical binding can be quantitatively examined using Berlin's theorem (Berlin, 1951), which uses the Hellman-Feynman approach to define binding and antibinding regions of a molecule. Electron density in the binding region holds the atoms together, whereas density in the antibinding region tends to pull them apart. As pointed out by Spackman and Maslen (1985), Berlin's theorem has at times been misused in interpreting maps of the deformation electron density. It is often assumed that an accumulation of deformation density between two atoms is required for bond formation. In reality such accumulation is neither necessary nor sufficient to bind the nuclei (Spackman and Maslen, 1985). This fact is most
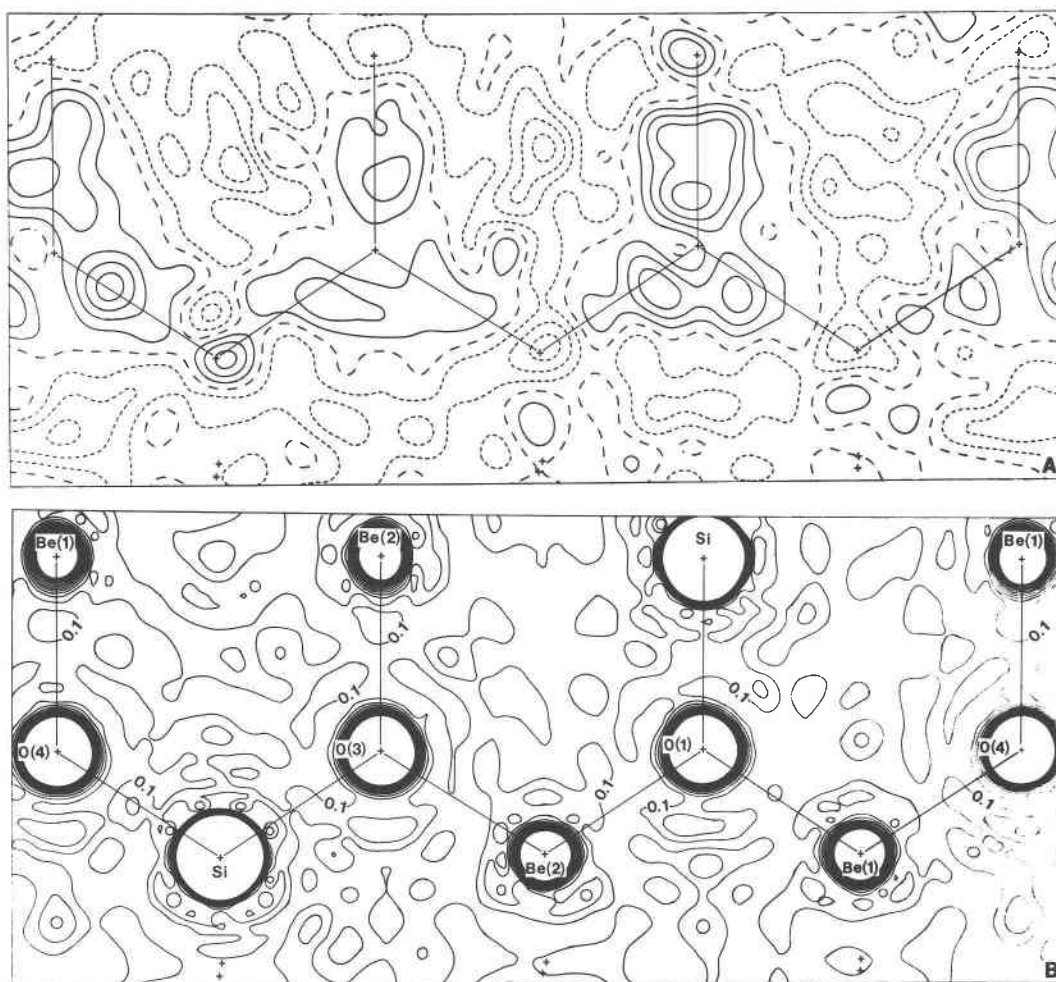
Fig. 2. (A) Dynamic deformation electron density in the plane of Figure 1. Solid contours positive (i.e., accumulation of electron density), small dashes negative; large dashes represent zero contour. Contour interval 0.1 e Å^{-3}. (B) Estimated standard deviation in deformation electron density. Contour interval 0.1 e Å^{-3}.

evident in theoretical deformation maps of the diatomics F_2 and O_2, which show large negative features in the deformation density along the bond and yet are bound species. Furthermore, Berlin's theorem shows that the most significant electron-density deformations, as far as binding is concerned, are very close to the nuclei. For N_2 and F_2, Spackman and Maslen (1985) have shown that the deformation density at the bond midpoint has almost no effect on the binding of the nuclei.

In light of the above, we do not insist that positive deformation density between nearest neighbors implies bonds or that larger accumulations of deformation density imply greater binding. We merely observe that large deformation-density accumulations appear to be associated with short interatomic distances in phenakite.

As pointed out by Bader (1981), the concepts of covalent vs. ionic character of a bond originate in valence-bond theory where the total wavefunction of a molecule is considered as the combination of a fully covalent and a fully ionic wavefunction. The percentage contribution

of the ionic wavefunction to the total wavefunction is one definition of the ionic character. The electronegativity difference between two bonded atoms is closely related to the importance of the ionic portion of a valence-bond wavefunction. Electronegativity differences have therefore been used to predict ionic or covalent character, which is essentially an attempt to empirically predict the nature of an electron distribution. When an accurate electron density has been either calculated or observed, the concepts of covalent vs. ionic character become less necessary. One problem with the concepts of ionicity or covalency is that, along with atomic size, charge, and coordination number, these properties are not quantum mechanical observables. In other words, there are no quantum mechanical operators that may operate on the total wavefunction to uniquely yield these properties. Properties such as the electronic energy, electric fields, electric-field gradients, etc., are rigorously defined in terms of the wavefunction.

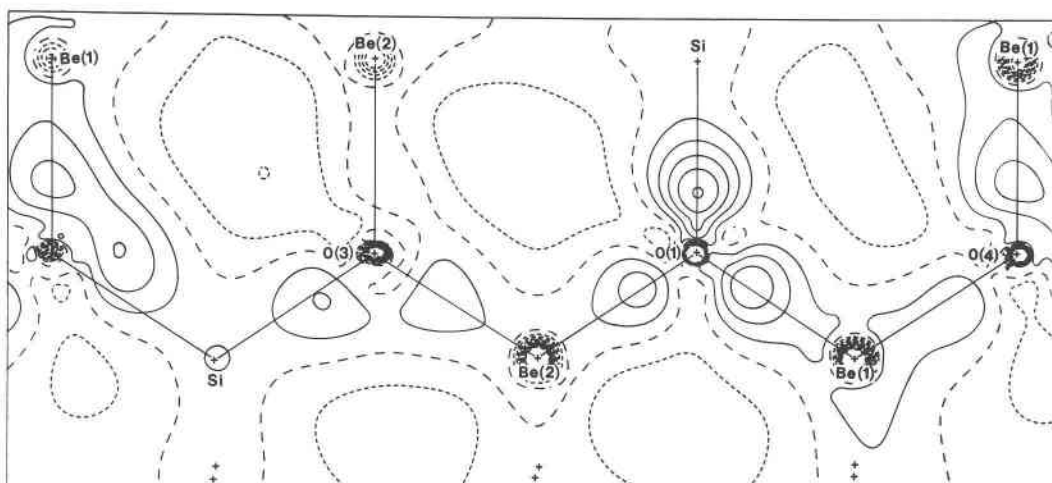If the deformation electron density of a molecule for

Fig. 3. Static deformation density computed in direct space from a superposition of spherical GSFs and multipole deformation functions. Contour interval 0.1 e Å⁻³.

which the valence-bond wavefunction shows a high degree of ionic character (e.g., LiF) is observed, the zero contour will tend to be spherical, and more importantly, will completely enclose the anion. Bader (1981) has emphasized that the words *ionic* and *covalent* can be used in a nonpredictive sense to describe an observed electron-density distribution. The zero contours in Figure 2A are seen to nearly enclose each oxygen atom. Furthermore, the peaks in the deformation density are closer to oxygen than to their nearest neighbors. This is consistent with the higher electronegativity of oxygen compared to that of Be or Si. Thus, in a qualitative sense, the deformation density of phenakite appears to exhibit a good deal of ionic character. However, assuming there has been a net charge transfer to oxygen, the oxygen anions are polarized toward the cations, indicating substantial covalency in these bonds.

A map of the *static deformation density* is shown in Figure 3. This map is not generated by Fourier series but is calculated from the monopole terms and refined higher multipole functions in direct space. The electron densities of static, spherical atoms are subtracted to form the deformation density. Since the multipoles are assumed to rigidly follow the nuclear motion, it is assumed that the effect of nuclear vibrations has largely been removed. In making this statement it is assumed that the scattering model is correct so that the refined vibrational parameters will be reliable. Although the map looks somewhat different from the *dynamic deformation density* shown in Figure 2, most bonds still exhibit an accumulation of deformation density.

It may appear surprising that the static deformation density about O(3) shows less accumulation than the vibrationally smeared density. This could be because the same fixed monopole GSF is used for all oxygen atoms; this fact means that any variations must be fit by the higher multipoles, which cannot bring about a charge

transfer between pseudoatoms. This result may also be due to the nonideal quality of the low-order data, wherein sufficient noise makes an accurate multipole fit difficult to obtain.

It is noteworthy that O(1) exhibits larger deformation-density features and shorter bonds than O(3) in both the dynamic and static maps. The question arises as to whether O(1) could have a greater ionic charge than O(3). It is tempting to use the kappa charges for this purpose. However, kappa charges are never sufficient to address such a question, which requires a more sophisticated definition and measurement of atomic charge using a substantially more accurate pseudoatom fit than that presented here.

Electrostatic potential

Another electrostatic property of interest is the total electrostatic potential. A map of the electrostatic potential gives the negative work done by a positive charge to come from infinity to a given point on the map. Such a map is shown in Figure 4 for the same plane viewed in Figures 2 and 3. The map is calculated with a combination of Fourier series and direct-space methods as discussed by Stewart (1979) and Spackman and Stewart (1981). Negative contours are dashed and show where a positive charge would be attracted by the electrostatic potential. Since the potential is singular at the nuclear positions, the positive contours near these positions are omitted. Figure 4B is a map of the estimated standard deviation of the total electrostatic potential and indicates that this property is of most interest in the internuclear regions where the error is about 0.1 e/Å.

One can almost see *atoms* in the total potential map. This is because the zero contour nearly envelops each nucleus in a roughly spherical fashion. The atomic sizes depicted here are clearly not what are normally represented in introductory mineralogy texts where Be and Si
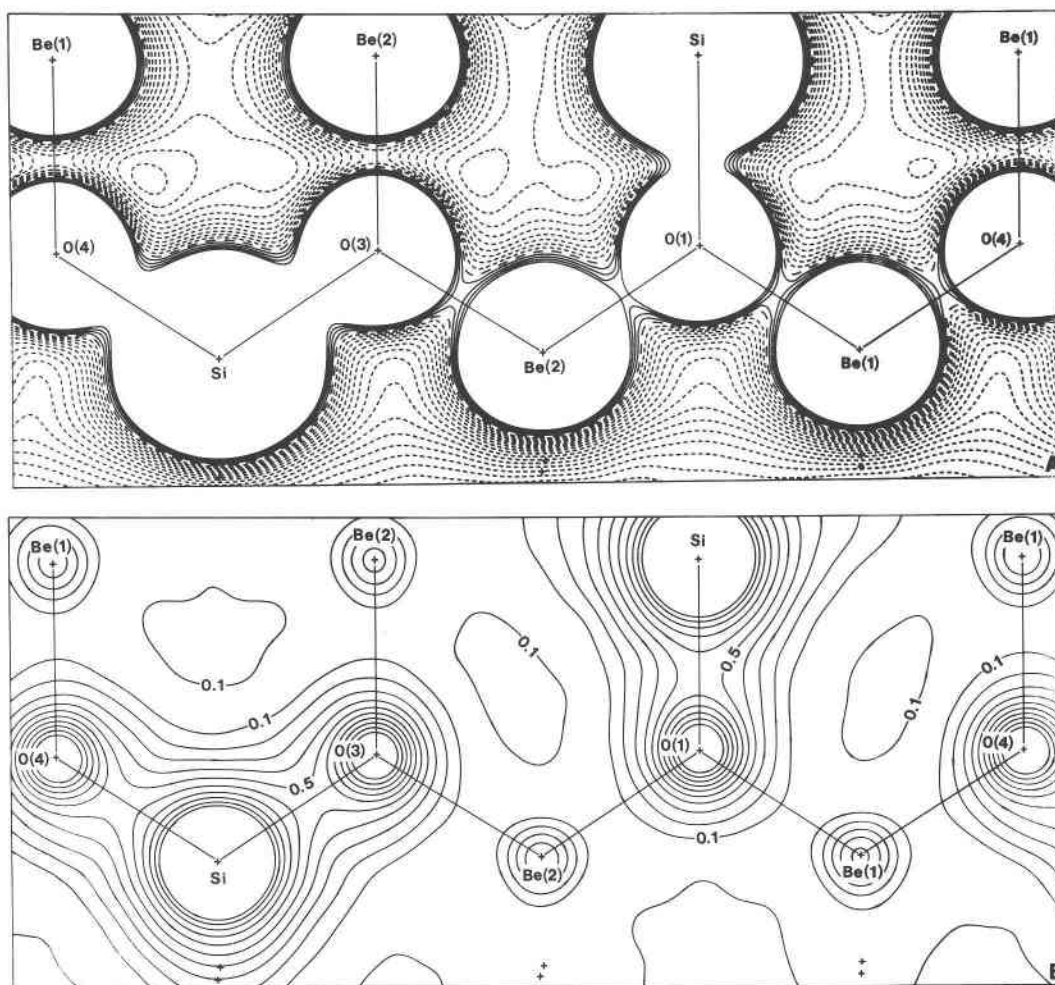
Fig. 4.   (A) Total electrostatic potential in plane of Figure 2. Small dashes negative, large dashes zero; solid contours are positive and have not been plotted near nuclear positions. Contour interval 0.1 e Å⁻¹(1 e Å⁻¹ = 14.4 eV/unit charge = 1389 kJ/mol = 332.1 kcal/mol). (B) Estimated standard deviation of total electrostatic potential. Contour interval is 0.1 e Å⁻¹.

are usually represented as small cations and oxygens are large anions. In one of the first papers on the sizes of ions, Linus Pauling (1928) said, "The electron density of an ion remains finite even at very large distances from the nucleus, and shows no discontinuities. Hence it is not possible to assign one radius to each ion and call it the true radius; instead, various radii may be assigned each ion, each one of interest with reference to a particular physical property." The effective ionic radii of Shannon and Prewitt (1969), the atomic radii of Slater (1965), and the *potential radii* evident in Figure 4 are clearly based on different criteria.

As with all potentials, the electrostatic potential is given to within a constant factor. In a crystal, this factor is chosen so that the unit cell is electrostatically neutral, whereas for an isolated molecule, the integral of the potential throughout all space must vanish. Therefore, potential radii can never be absolute.

One useful feature of viewing atomic size through the electrostatic potential is that this property includes the effects of the nuclear charge distribution as well as the electron distribution. This is important when considering transport and catalytic properties since any atom or molecule within a crystal must interact with the *total* charge distribution. The total electrostatic potential may therefore yield a more realistic picture of the sizes of interacting atoms than does the total electron density or deformation density.

Zachariasen (1972) first noted the rather short metal-metal distances parallel to Z (Fig. 1) and suggested that this direction could be one of low compressibility. Recent high-pressure studies by Kogure and Takéuchi (1986) yield nearly equal compressibilities for c and a, with only a slight increase in c/a with increasing pressure, supporting Zachariasen's conclusion.

In a qualitative sense, the compressed nature of the structure along Z is evident in the map of the electrostatic potential. The internuclear vectors connecting O(4)–Si–O(3)–Be(2)–O(1)–Be(1)–O(4) lie along a ridge of continuously positive potential. Normal to Z, negative potential

occurs in the middle of the Be(1)–O(4) and Be(2)–O(3) bonds, and the potential in the Si–O(1) bond is less electropositive than that in the Si–O(3) bond.

CONCLUSIONS

We have presented the results of an attempt to extract the deformation electron density and total electrostatic potential of phenakite from X-ray diffraction data. Although the data are not of the superior quality required for an extensive and quantitative charge-density analysis, a few conclusions can be reached.

1. The dynamic deformation electron density of phenakite exhibits accumulations of electron density between nearest-neighbor atoms, with shorter bonds showing larger accumulation than long bonds between atoms of similar type.

2. The zero contour in the deformation density virtually encloses each oxygen nucleus, thus classifying the deformation density with that of molecules having a large ionic component to the bonding, such as LiF. However, the electron density within this contour is not spherical, but is polarized toward the cation nuclei, indicating a substantial covalent component as well. A theoretical model of fully ionized atoms, which show no polarization, may not be an accurate electron-density model for phenakite.

3. From the viewpoint of a positive test charge, the electrostatic potential shows that Si and Be are large relative to oxygen in phenakite. The conventional picture of tiny Be and Si cations surrounded by large oxygen anions may not be the most realistic when considering properties such as diffusion or catalytic activity.

4. The dense packing of the phenakite structure parallel to the Z axis appears obvious from the electrostatic potential, in agreement with the conclusions of Zachariasen (1972), Hazen and Au (1986), and Kogure and Takéuchi (1986).

ACKNOWLEDGMENTS

REFERENCES

Bader, R.F.W. (1981) The nature of chemical binding. In B.M. Deb, Ed., The force concept in chemistry, p. 39–136. Van Nostrand Reinhold, New York.

Becker, P.J., and Coppens, P. (1974a) Extinction within the limit of validity of the Darwin transfer equations. I. General formalisms for primary and secondary extinction and their application to spherical crystals. Acta Crystallographica, A30, 129–147.

——— (1974b) Extinction within the limit of validity of the Darwin transfer equations. II. Refinement of extinction in spherical crystals of SrF$_2$ and LiF. Acta Crystallographica, A30, 148–153.

Berlin, T. (1951) Binding regions in diatomic molecules. Journal of Chemical Physics, 19, 208–213.

Blessing, R.H., Coppens, P., and Becker P. (1974) Computer analysis of step-scanned X-ray data. Journal of Applied Crystallography, 7, 488–492.

Bragg, W.L., and Zachariasen, W.H. (1930) The crystalline structure of phenacite, Be$_2$SiO$_4$, and willemite, Zn$_2$SiO$_4$. Zeitschrift für Kristallographie, 72, 518–528.

Clementi, E., and Roetti, C. (1974) Roothaan-Hartree-Fock wavefunctions: Basis functions and their coefficients for ground and certain excited states of neutral and ionized atoms, Z < 54. Atomic Data and Nuclear Data Tables, 14, 177–478.

Coppens, P. (1977) Overcoming the free-atom bias in modified least-squares formalisms. Israel Journal of Chemistry, 16, 159–162.

Cromer, D.T., and Liberman, D. (1970) Relativistic calculations of anomalous scattering factors for X-rays. Journal of Chemical Physics, 53, 1891–1898.

Downs, J.W. (1983) An experimental examination of the electron distributions in bromellite, BeO, and phenacite, Be$_2$SiO$_4$. Ph.D. Dissertation, Virginia Polytechnic Institute and State University, Blacksburg, Virginia.

Feynman, R.P. (1939) Forces in molecules. Physical Review, 56, 340–343.

Hamilton, W.C. (1974) Angle settings for four-circle diffractometers. In International tables for X-ray crystallography, vol. IV, p. 273–284, Kynoch Press. (Present distributor D. Reidel, Dordrecht, The Netherlands.)

Hazen, R.M., and Au, A.Y. (1986) High-pressure crystal chemistry of phenakite (Be$_2$SiO$_4$) and bertrandite (Be$_4$Si$_2$O$_7$(OH)$_2$). Physics and Chemistry of Minerals, 13, 69–78.

Hazen, R.M., and Finger, L.W. (1987) High-temperature crystal chemistry of phenacite (Be$_2$SiO$_4$) and chrysoberyl (BeAl$_2$O$_4$). Physics and Chemistry of Minerals, in press.

Hirshfeld, F.L., and Rzotkiewicz, S. (1974) Electrostatic binding in the first-row AH and A$_2$ diatomic molecules. Molecular Physics, 27, 1319–1343.

Hohenberg, P., and Kohn, W. (1964) Inhomogeneous electron gas. Physical Review, 136 (3B), 864–871.

Kogure, T., and Takéuchi, Y. (1986) Compressibility of the BeO$_4$ tetrahedra in the crystal structure of phenacite. Mineralogical Journal, 13, 22–27.

Lehmann, M.S., and Larsen, F.K. (1974) A method for location of the peaks in step-scan–measured Bragg reflexions. Acta Crystallographica, A30, 580–584.

Pauling, L. (1928) The sizes of ions and their influence on the properties of salt-like compounds. Zeitschrift für Kristallographie, 67, 377–404.

Shannon, R.D., and Prewitt, C.T. (1969) Effective ionic radii in oxides and fluorides. Acta Crystallographica, B25, 925–946.

Slater, J.C. (1965) Quantum theory of molecules and solids, vol. 2. McGraw-Hill, New York.

Spackman, M.A., and Maslen, E.N. (1985) Electron density and the chemical bond. A reappraisal of Berlin's theorem. Acta Crystallographica, A41, 347–353.

Spackman, M.A., and Stewart, R.F. (1981) Electrostatic potentials in crystals. In P. Politzer and D. G. Truhlar, Eds., Chemical applications of atomic and molecular electrostatic potentials, p. 407–425. Plenum Press, New York.

Stewart, R.F. (1976) Electron population analysis with rigid pseudoatoms. Acta Crystallographica, A32, 565–574.

——— (1979) On the mapping of electrostatic properties from Bragg diffraction data. Chemical Physics Letters, 65, 335–342.

——— (1980) Partitioning of Hartree-Fock atomic form factors into core and valence shells. In P. Becker, Ed., Electron and magnetization densities in molecules and crystals, p. 427–431. Plenum Press, New York.

Stewart, R.F., and Spackman, M.A. (1983) VALRAY users manual. Department of Chemistry, Carnegie-Mellon University, Pittsburgh, Pennsylvania.

Stewart, R.F., Bentley, J., and Goodman, G. (1975) Generalized X-ray scattering factors in diatomic molecules. Journal of Chemical Physics, 63, 3786–3793.

Zachariasen, W.H. (1972) Refined crystal structure of phenacite Be$_2$SiO$_4$. Soviet Physics—Crystallography, 16, 1021–1025.